Scaffold subunits support associated subunit assembly in the *Chlamydomonas* ciliary nexin–dynein regulatory complex

Long Gui[a,b], Kangkang Song[a,b,1], Douglas Tritschler[c], Raqual Bower[c], Si Yan[a,b], Aguang Dai[a,b], Katherine Augspurger[c], Jason Sakizadeh[c], Magdalena Grzemska[a,b], Thomas Ni[a,b], Mary E. Porter[c,2], and Daniela Nicastro[a,b,2]

[a]Department of Cell Biology, University of Texas Southwestern Medical Center, Dallas, TX 75390; [b]Department of Biophysics, University of Texas Southwestern Medical Center, Dallas, TX 75390; and [c]Department of Genetics, Cell Biology, and Development, University of Minnesota Medical School, Minneapolis, MN 55455

Edited by Elizabeth Villa, University of California San Diego, La Jolla, CA, and accepted by Editorial Board Member John W. Sedat October 3, 2019 (received for review June 26, 2019)

The nexin–dynein regulatory complex (N-DRC) in motile cilia and flagella functions as a linker between neighboring doublet microtubules, acts to stabilize the axonemal core structure, and serves as a central hub for the regulation of ciliary motility. Although the N-DRC has been studied extensively using genetic, biochemical, and structural approaches, the precise arrangement of the 11 (or more) N-DRC subunits remains unknown. Here, using cryo-electron tomography, we have compared the structure of *Chlamydomonas* wild-type flagella to that of strains with specific DRC subunit deletions or rescued strains with tagged DRC subunits. Our results show that DRC7 is a central linker subunit that helps connect the N-DRC to the outer dynein arms. DRC11 is required for the assembly of DRC8, and DRC8/11 form a subcomplex in the proximal lobe of the linker domain that is required to form stable contacts to the neighboring B-tubule. Gold labeling of tagged subunits determines the precise locations of the previously ambiguous N terminus of DRC4 and C terminus of DRC5. DRC4 is now shown to contribute to the core scaffold of the N-DRC. Our results reveal the overall architecture of N-DRC, with the 3 subunits DRC1/2/4 forming a core complex that serves as the scaffold for the assembly of the "functional subunits," namely DRC3/5–8/11. These findings shed light on N-DRC assembly and its role in regulating flagellar beating.

cilia | flagella | cryo-electron tomography | N-DRC | axoneme

Cilia and flagella are dynamic microtubule (MT)-based organelles that emanate from the surface of many eukaryotic cells and are involved in sensory functions, motility, and signaling. Defects in cilia assembly or function have been associated with multiple human disorders collectively known as ciliopathies, such as polycystic kidney disease, Bardet–Biedl syndrome, infertility, hydrocephalus, and primary ciliary dyskinesia (1, 2).

The MT-based axoneme forms the core structure of motile cilia and is highly conserved, from the green algae *Chlamydomonas reinhardtii* to differentiated cells in the human body. The "9 + 2" axoneme is composed of 9 outer doublet MTs (DMTs) and a central-pair complex (CPC) composed of 2 singlet MTs and associated projections (Fig. 1*A*). Each DMT is built from many copies of a 96-nm-long unit that repeats along the length of the axoneme and consists of an A-tubule and B-tubule. The outer and inner dynein arms (ODAs and IDAs, respectively) are arranged in 2 distinct rows along the length of the A-tubule of each DMT and function as the motors that drive ciliary motility. The dynein motors "walk" on the B-tubule of the neighboring DMT and thereby generate sliding forces between the doublets (3). The nexin link between DMTs is thought to restrict this interdoublet sliding and thus transform sliding into axonemal bending (4–6). Our previous ultrastructural study demonstrated that the nexin link is an integral part of the dynein regulatory complex, referred to as the nexin–dynein regulatory complex (N-DRC) (7). Formation of ciliary bending in different directions and beating patterns require precise regulation and coordination of the activities of thousands of axonemal dyneins (8–10). Genetic, biochemical, and structural studies suggest that several complexes are involved in the transduction of signals that ultimately control the activity of the dyneins. These regulatory complexes include the CPC, the radial spokes, the calmodulin- and radial spoke-associated complex (CSC), the I1 inner dynein (or dynein f) on the proximal end of the 96-nm axonemal repeat, and the N-DRC on the distal end of the repeat (11).

The N-DRC is a large 1.5-MDa structure consisting of 2 main domains, the base plate and the linker (Fig. 1*C*). The base plate attaches to the DMT, beginning at the inner junction between the A- and B-tubule and ending at protofilament A4. The linker domain extends across the interdoublet space to the neighboring B-tubule (7). Genetic and biochemical studies have demonstrated that the N-DRC is composed of at least 11 subunits, but the precise arrangement of these subunits in the N-DRC structure

Significance

Cilia and flagella are small hair-like appendages in eukaryotic cells that play essential roles in cell sensing, signaling, and motility. The highly conserved nexin–dynein regulatory complex (N-DRC) is one of the key regulators for ciliary motility. At least 11 proteins (DRC1–11) have been assigned to the N-DRC, but their precise arrangement within the large N-DRC structure is not yet known. Here, using cryo-electron tomography combined with genetic approaches, we have localized DRC7, the subcomplex DRC8/DRC11, the N terminus of DRC4, and the C terminus of DRC5. Our results provide insights into N-DRC structure, its function in the regulation of dynein activity, and the mechanism by which *n-drc* mutations can lead to defects in ciliary motility that cause disease.

Author contributions: M.E.P. and D.N. designed research; L.G., K.S., D.T., R.B., K.A., J.S., M.E.P., and D.N. performed research; L.G., K.S., D.T., R.B., S.Y., A.D., M.G., T.N., M.E.P., and D.N. analyzed data; and L.G., M.E.P., and D.N. wrote the paper.

The authors declare no competing interest.

This article is a PNAS Direct Submission. E.V. is a guest editor invited by the Editorial Board.

Data deposition: The 3-dimensional averaged structures of 96-nm axonemal repeats reported in this paper have been deposited in the Electron Microscopy Data Bank, https://www.ebi.ac.uk/pdbe/emdb (accession codes EMD-20338, EMD-20339, EMD-20340, EMD-20341, and EMD-20821).

[1]Present address: Biochemistry and Molecular Pharmacology, University of Massachusetts Medical School, Worcester, MA 01655.

[2]To whom correspondence may be addressed. Email: porte001@umn.edu or daniela.nicastro@utsouthwestern.edu.

This article contains supporting information online at www.pnas.org/lookup/suppl/doi:10.1073/pnas.1910960116/-/DCSupplemental.

First published October 28, 2019.

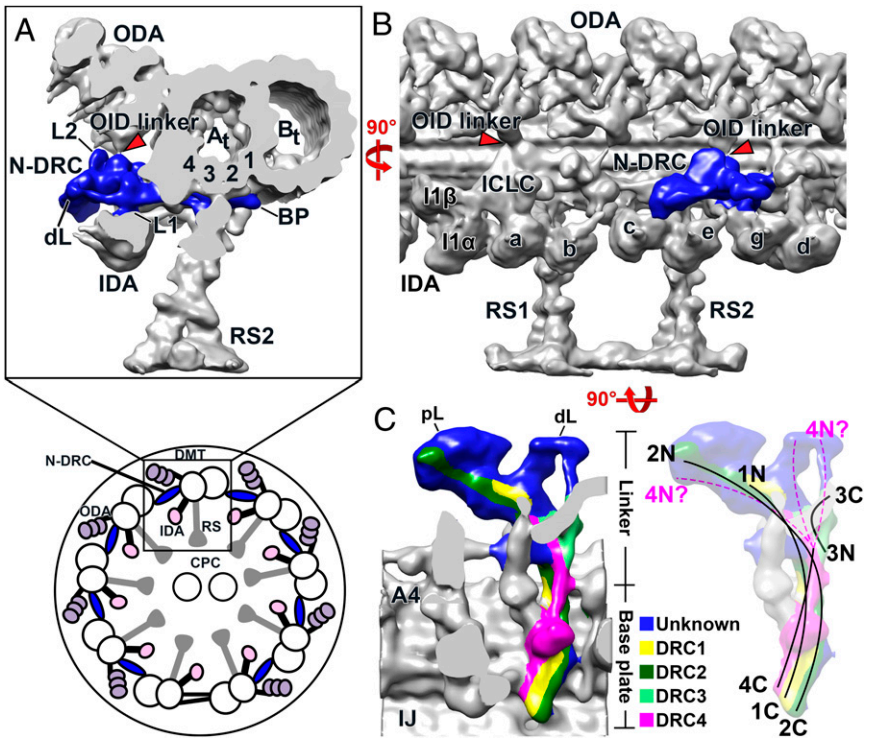

Fig. 1. Structure of the N-DRC and organization of known N-DRC subunits in *Chlamydomonas* flagella. (*A*–*C*) Schematic of a *Chlamydomonas* flagellum in cross-sectional view (*A*, *Bottom*), seen from the flagellar tip toward the base. The outer and inner dynein arms (ODA, IDA) and the nexin–dynein regulatory complex (N-DRC) connect the neighboring doublet microtubules (DMTs), whereas the radial spokes (RSs) connect to the central-pair complex (CPC). (*A*, *Top*, *B*, and *C*) Isosurface rendering of the 3D structure of the 96-nm axonemal repeat in *Chlamydomonas* WT flagella reconstructed by cryo-electron tomography (cryo-ET), shown in cross-sectional (*A*, *Top*), longitudinal front (*B*), and bottom views (*C*). (*A*, *Top* and *B*) Overviews showing the location of the N-DRC (blue) within the axonemal repeat, and connections between the N-DRC and other axonemal structures, including the outer dynein/inner dynein (OID) linkers (red arrowheads). The N-DRC linker region has 3 protrusions: the L1 and L2 protrusions, and the OID linker. (*C*) Three-dimensional maps of the N-DRC in longitudinal views from the bottom. The known locations of DRC1–4 (1–4) are colored; N and C correspond to the N and C termini of the proteins, respectively. The dashed line indicates ambiguity in localization of the N-terminal region of DRC4. Note that DRC5 and DRC6 are thought to be located at the L2 projection, which is in the dorsal side of the linker and thus cannot be visualized in *C*. Other labels: A_t, A-tubule (protofilaments 1 to 4 are labeled in *A*, *Top*, and A4 in *C*); B_t, B-tubule; BP, base plate; dL, distal lobe; I1α/I1β/ICLC, α- and β-heavy chain, and intermediate/light-chain complex of I1 dynein; IJ, inner junction; a–e and g, inner dynein arm isoforms; pL, proximal lobe.

remains elusive (12, 13). Recent work with tagged subunits has revealed the approximate locations of DRC1–6. The C termini of DRC1, DRC2(FAP250), and DRC4 are located close to each other at the end of the base plate near the inner junction, and their N termini extend through the linker toward the neighboring B-tubule. DRC3(FAP134), DRC5(FAP155), and DRC6(FAP169) are located in the linker region (7, 14–16). However, little is yet known about the locations of DRC7-11 or the specific interactions within the structure of the N-DRC. The identification of DRC7-11 mutants will be important for the dissection of the N-DRC and its function as regulatory hub.

Here, we have integrated genetic and biochemical approaches with cryo-electron tomography (cryo-ET) to localize DRC7 (FAP50) and the subcomplex DRC8/11 (FAP200/FAP82) within the N-DRC. DRC7 is found in the central region of the N-DRC linker, including the outer dynein/inner dynein (OID) linker between the N-DRC and the row of outer dynein arms (Fig. 1*B*). The *drc11* mutant lacks 2 N-DRC subunits: DRC11 and DRC8, which localize to the proximal lobe of the N-DRC linker domain. We also use cryo-ET of SNAP-tagged DRCs to precisely locate the C terminus of DRC5 in the middle region of the linker, and the N terminus of DRC4 to the proximal lobe of the linker domain.

Results

Identification of *drc* Mutants for DRC7 and DRC11. The N-DRC contains at least 11 DRC subunits with distinct functional domains, but *drc* mutations have only been characterized in 5 genes (*drc1-drc5*) in *Chlamydomonas*. To extend the repertoire of *drc* mutants, we analyzed a collection of mutants generated by insertional mutagenesis the *Chlamydomonas* Library Project (CLiP) (17, 18) (*SI Appendix*, *SI Materials and Methods*). PCR confirmed the sites of plasmid insertion in 2 *drc7* strains and 2 *drc11* strains; however, the impact of plasmid insertion was highly variable (*SI Appendix*, Table S1 and Fig. S1).

None of the *drc7* strains examined displayed an obvious motility defect by phase contrast light microscopy (Fig. 2*B* and *SI Appendix*, Table S1), and so axonemes were isolated from 2 strains and analyzed on Western blots. No DRC7 band was detected in the 197909 strain (from now on referred to as *drc7*) (Fig. 2*C*), whereas strain 080526 showed 2 DRC7-related bands (*SI Appendix*, Fig. S1*D*) that are likely the result of alternative splicing. To determine whether the absence of DRC7 affected the assembly of other axonemal proteins, the *drc7* axonemes were labeled with isobaric tags for relative and absolute quantitation (iTRAQ) and analyzed by tandem mass spectrometry (MS/MS). Between about 500 and 650 proteins were identified by at least 5 peptides in 2 independent iTRAQ experiments. However, only one protein, DRC7, was significantly reduced ($P < 0.05$) below 50% in both experiments (*SI Appendix*, Table S2). All of the other DRC subunits were present at wild-type (WT) levels (*SI Appendix*, Table S2), as confirmed by Western blots (Fig. 2*C*).

Although both *drc11* candidates had confirmed plasmid insertions in introns (*SI Appendix*, Fig. S1 *E*–*G*), they displayed different motility phenotypes. The 130937 strain displayed an obvious slow swimming phenotype (*SI Appendix*, Fig. S2*B*) and failed to assemble both DRC11 and DRC8 (*SI Appendix*, Fig. S2*C*). However, transformation with a BAC clone (39g16) containing the *DRC11* gene failed to rescue the motility defect (0 rescues out of 538 transformants). This observation suggested the possibility of a second motility mutation in this strain. Further analysis by iTRAQ labeling, MS/MS, Western blots, and cryo-ET revealed that the *drc11-937* strain contained an unmapped mutation in a gene that disrupted the assembly of the outer dynein arms (*SI Appendix*, Fig. S2 *C*–*I* and Table S3).

The second *drc11* strain, 068819, displayed a slight but significant decrease in its forward swimming velocity (Fig. 2*B*). Western blots of axonemes confirmed that both DRC11 and DRC8 were missing, but several other DRC subunits and the outer dynein arms (as detected by an IC2/IC69 antibody) were present at WT levels (Fig. 2*D*). To determine whether the loss of DRC8 and DRC11 affected the assembly of other polypeptides, the 068819 axonemes were analyzed by iTRAQ labeling and MS/MS.

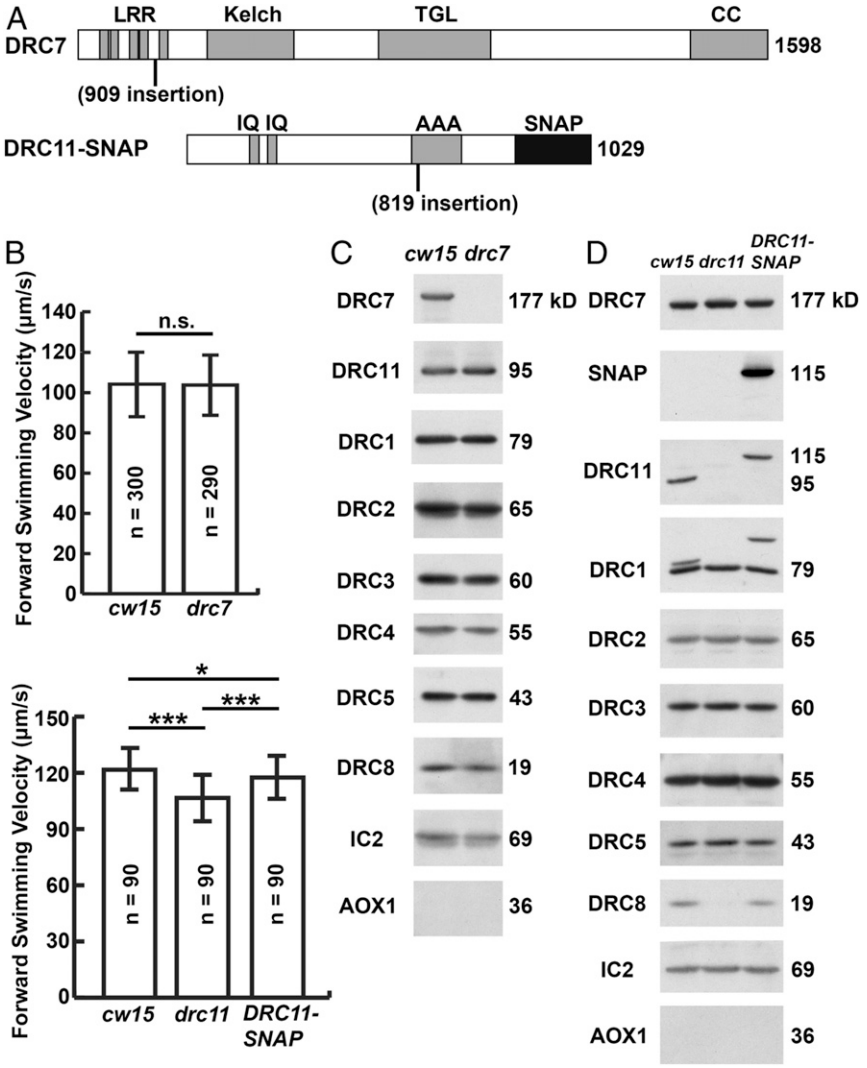

Fig. 2. Characterization of recently isolated mutations in *DRC7* and *DRC11*, and their impact on flagellar motility and assembly of the N-DRC. (*A*) The DRC7 and DRC11 protein sequences are drawn to scale, with the location of predicted polypeptide domains indicated: AAA, ATPase associated with diverse cellular activities domain; CC, coiled-coil domain; IQ, calmodulin binding domain; Kelch, Kelch domain; LRR, leucine-rich repeat; SNAP, C-terminal SNAP tag; TGL, transglutaminase-like domain. Also shown are the approximate locations of the plasmid insertion sites in the *drc7* and *drc11* mutants. (*B*) The forward swimming velocities of *drc7* and *drc11* as measured by phase contrast microscopy are shown relative to the background strain (*cw15*). No significant difference was detected between *drc7* and *cw15*. The *drc11* strain was slightly slower than *cw15*, and transformation with a tagged WT gene, *DRC11-SNAP*, increased swimming velocities to near *cw15* levels. $*P < 0.05$; $***P < 0.001$; n.s., not significant ($P > 0.05$). (*C* and *D*) Western blots of axonemes isolated from the "WT" background (*cw15*), the *drc* mutants, and the *DRC11-SNAP* rescued strain were probed with antibodies against several DRC subunits. Note the presence of a band detected by both the DRC11 and SNAP antibodies that migrated at the size predicted for a SNAP-tagged DRC11 subunit in *D*. Note that the DRC11 blot in *D* was reprobed with the DRC1 antibody, so that the blot shown for DRC1 (immediately below DRC11) shows not only the DRC1 bands in all lanes, but also the DRC11 (for cw15) and the DRC11-SNAP (for the rescue) bands. Antibodies against the IC2 subunit of the outer dynein arm served as a loading control, and antibodies against AOX1 served as a marker for cell body contamination.

Between about 530 and 630 proteins were identified by at least 5 peptides in 2 independent experiments. However, only 3 proteins were significantly reduced below 30% in both iTRAQ experiments (*SI Appendix*, Table S4): DRC8, DRC11, and Cre12.g513650. Little is known about Cre12.g513650; it is a small protein (146 amino acids) found only in green alga.

To verify that the defects observed in the 068819 strain were caused by the *drc11* mutation, we transformed the mutant with a WT *DRC11* cDNA containing a C-terminal SNAP tag (Fig. 2*A*). A SNAP-positive strain was recovered that increased forward swimming velocities to near WT levels (Fig. 2*B*) and restored the assembly of both DRC11 and DRC8, as shown by Western blots of axonemes (Fig. 2*D*). Furthermore, the DRC11-C-SNAP polypeptide migrated at the size expected for the SNAP-tagged protein (~115 kDa). These results demonstrate that the 068819 strain is a bona fide *drc11* mutation and that DRC8 depends on the presence of DRC11 for its assembly into the axoneme.

DRC7 Localizes to the N-DRC Linker Including the OID Linker and Distal Lobe. Three-dimensional reconstruction of the axoneme by cryo-ET and subtomogram averaging revealed that the N-DRC linker begins approximately at protofilament A4 and projects into space between neighboring doublets (Fig. 1 *A* and *C*) (7, 19). The linker domain contains several protrusions: L1 that connects to IDA g, L2 at the branch point between the proximal and distal lobes, and the OID linker that connects the N-DRC to the ODAs (Fig. 1*A*). The proximal lobe is at least twice as the size of the distal lobe, but they both connect to the neighboring B-tubule (Fig. 1*C*).

To determine the location of DRC7 subunit, we compared the 3D structure of WT and *drc7* axonemes by cryo-ET and subtomogram averaging (Fig. 3). We found missing densities only within the N-DRC linker domain and not in the base plate. Specifically, the *drc7* N-DRC lacks the OID linker, a density on the distal side of the linker, and the most distal portion of the distal lobe (Fig. 3 *D*–F and J–L and Movie S1), which reduces the size of the distal lobe interface with the neighboring B-tubule. The total mass of the densities missing in the *drc7* N-DRC is estimated to be ~200 kDa, suggesting that the density contains a single copy of DRC7, which has a molecular weight of 177 kDa.

DRC8/11 Localize to the Proximal Lobe of the N-DRC Linker. Our biochemical assays have indicated that the *drc11* strain lacks 2 polypeptides, DRC8 and DRC11. To determine the location of the DRC8/11 subcomplex, we analyzed *drc11* axonemes by cryo-ET and subtomogram averaging (Fig. 4). Compared with wild type, the averaged 96-nm repeats of *drc11* axonemes showed deficiencies in the proximal lobe of the N-DRC linker region (Fig. 4 *D*–*F* and *J*–*L* and Movie S2). The structural defect greatly reduces the interface between the proximal lobe and the neighboring B-tubule. The missing density is estimated to be ~250 kDa. The morphology

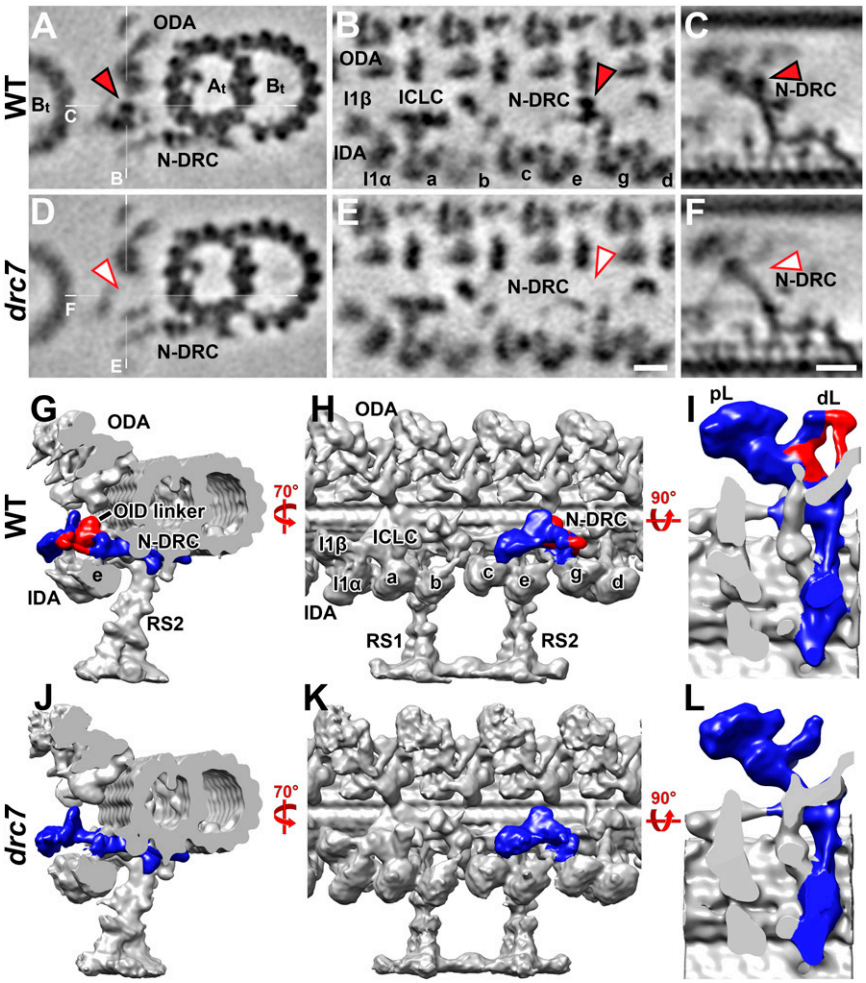

Fig. 3. Comparison between WT and *drc7* axonemes reveals the location of DRC7 near the OID linker and in part of the distal lobe of the N-DRC. (*A–F*) Tomographic slices of the averaged 96-nm-long repeats from *Chlamydomonas* WT (*A–C*) and *drc7* axonemes (*D–F*) viewed in cross-sectional (*A* and *D*) and longitudinal (*B*, *C*, *E*, and *F*) orientations. The white lines indicate the locations of the slices in the respective panels. Cryo-ET densities corresponding to DRC7 in the nexin–dynein regulatory complex (N-DRC) of WT (red arrowheads in *A–C*) were absent from *drc7* axonemes (white arrowheads in *D–F*). (*G–L*) Isosurface renderings show the 3D structures of the averaged axonemal repeats of WT (*G–I*) and *drc7* (*J–L*) in cross-sectional (*G* and *J*), longitudinal (*H* and *K*), and enlarged longitudinal bottom views (*I* and *L*; looking from the axoneme center outward). The structural difference between the WT and *drc7* is manually colored red in *G–I* and includes the OID linker, a portion of the distal lobe (dL), and the connection between the distal lobe and the L1 protrusion (named connection 7 in ref. 7). Other labels: a–e and g, inner dynein arm isoforms; A_t, A-tubule; B_t, B-tubule; I1α/I1β/ICLC, α- and β-heavy chain, and intermediate/light-chain complex of I1 dynein; IDA, inner dynein arm; ODA, outer dynein arm; pL, proximal lobe; RS, radial spoke. (Scale bar: 10 nm [in *E*, valid also for *A*, *B*, and *D*]; 10 nm [in *F*, valid also for *C*].)

of the other N-DRC domains, including the distal lobe and the base plate, resembled the WT structure. Although we found that strain *drc11-937* was a double mutant with additional ODA defects, we were still able to detect the same N-DRC structural defects in this double mutant (*SI Appendix*, Fig. S2 *C–I*) as described for *drc11*.

The tip region (close to the neighboring DMT) and the upper part of the proximal lobe (facing the ODA) were completely missing in *drc11* axonemes. In addition, we observed a remaining, yet weakened and blurred cryo-ET density that appears to be the lower portion of the proximal lobe that faces the IDAs (Fig. 5 *B* and *G*). This blurring effect could be due to reduced occupancy or positional flexibility of the structures that comprise this region. Therefore, we applied automatic image classification analyses with different masks that focused the analyses on specific structures of interest (20). Classification of WT repeats showed one structurally homogenous state across all of the axonemal repeats (Fig. 5 *A* and *F*). In contrast, we found that the lower proximal lobe structure in *drc11* fell into 4 conformational classes, which differed mainly in its position ("height") between the ODA and IDA rows (Fig. 5 and Movie S3). More specifically, 23% of the repeats showed the remaining proximal lobe density in a low position close to the IDAs (class 1, Fig. 5 *C* and *H*); 25% were positioned in the middle (class 2, Fig. 5 *D* and *I*); and 27% were located in a higher position closer to the ODAs (class 3, Fig. 5 *E* and *J*). The remaining 25% could not be categorized because of blurred densities and anisotropic density distribution caused by the missing wedge-artifact typical for raw single-axis tomographic reconstructions (21). Thus, the proximal lobe of the N-DRC is composed of 2 parts: The DRC8/11 subcomplex comprises the tip and upper (ODA-facing) region of the proximal lobe, whereas the lower (IDA-facing) part of the proximal lobe likely contains the N-terminal regions of the "backbone subunits" DRC2 and DRC4.

Rescue of *drc4* and *drc5* Mutants with SNAP-Tagged Constructs Clarifies the Location of DRC4 and DRC5 in the N-DRC Linker. Previous studies focusing on DRC subunits DRC1–6 showed that DRC1, DRC2, and DRC4 are coiled-coil proteins that extend from the inner junction between the A- and B-tubule through the N-DRC base plate and linker to the neighboring DMT (7, 14, 16) (Fig. 1*C*). Mutations in these proteins disrupt the assembly of multiple DRC subunits (12, 13, 22–25). In contrast, DRC3, DRC5, and DRC6 are located in the N-DRC linker region, and defects in DRC3, DRC5, or DRC6 have only small effects on the assembly of other DRC subunits or the overall structure of the N-DRC (7, 12, 13, 15, 16). Rescues of various *drc* mutants with tagged WT *DRC* genes allowed the localization of the N- and/or C-termini of DRC1 (N/C), DRC2 (N/C), DRC3 (N/C), DRC4 (C), and DRC5 (C) (Fig. 1*C*, *Right*). For example, the SNAP-tagged N and C termini of DRC3 have been unambiguously located in the L1 projection of the N-DRC linker that connects to IDA g (16). However, tagging the N terminus of DRC4 with BCCP resulted in variable labeling throughout the proximal lobe. A C-terminal biotin carboxyl carrier protein (BCCP) tag of DRC5 appears to localize to the upper (ODA-facing) region of an unbranched part of the N-DRC linker, and the cryo-ET density corresponding to the tag at the C terminus of DRC5 was diffuse and blurred (7, 14).

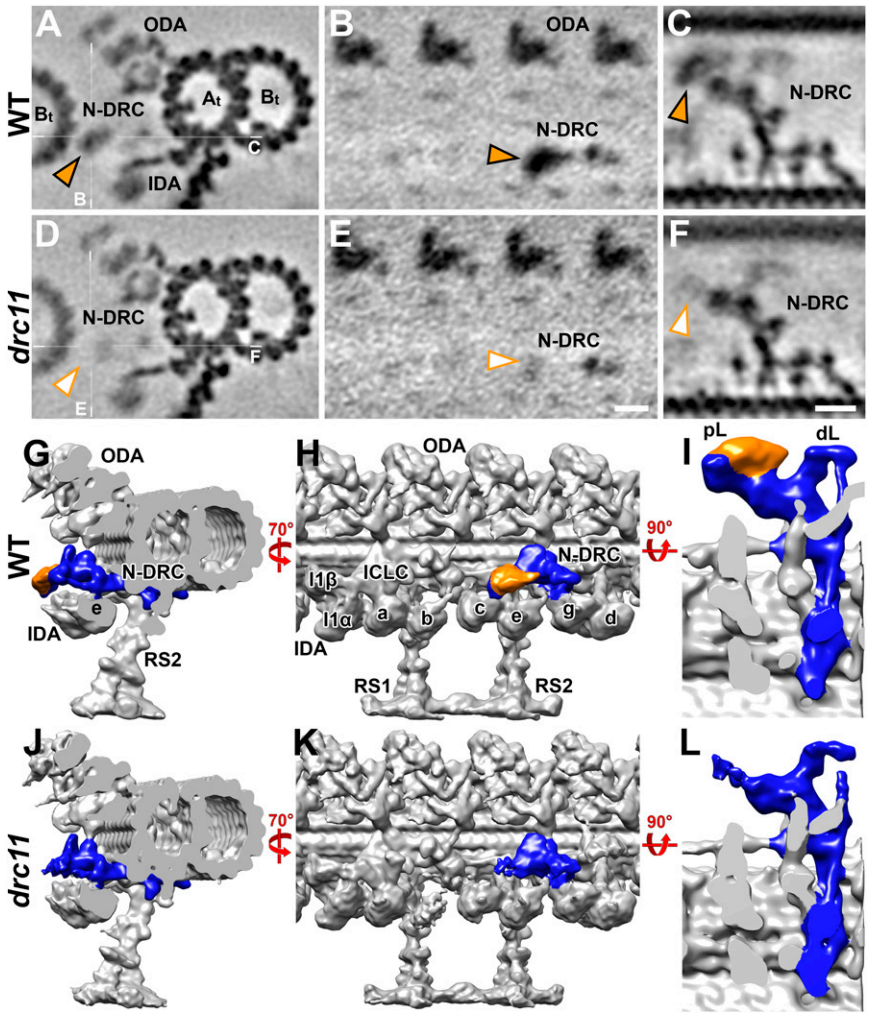

Fig. 4. Three-dimensional localization of the DRC8/11 subcomplex at the proximal lobe of the N-DRC linker using cryo-ET. (*A–F*) Tomographic slices of the averaged 96-nm repeats of *Chlamydomonas* WT (*A–C*) and *drc11* axonemes (*D–F*) viewed in cross-sectional (*A* and *D*) and longitudinal (*B*, *C*, *E*, and *F*) orientations. The white lines indicate the locations of the slices in the respective panels. Cryo-ET densities corresponding to DRC8/11 in the nexin–dynein regulatory complex (N-DRC) of WT (orange arrowheads in *A–C*) were missing from the *drc11* axonemes (white arrowheads in *D–F*). (*G–L*) Isosurface renderings show the 3D structures of the averaged axonemal repeats of WT (*G–I*) and *drc11* (*J–L*) in cross-sectional (*G* and *J*), longitudinal (*H* and *K*), and enlarged longitudinal bottom views (*I* and *L*; looking from the axoneme center outward). The structural difference between the WT and *drc11* is manually colored orange in *G–I* and includes a major portion of the proximal lobe (pL). Other labels: a–e and g, inner dynein arm isoforms; A_t, A-tubule; B_t, B-tubule; dL, distal lobe; I1α/I1β/ICLC, α- and β-heavy chain, and intermediate/light-chain complex of I1 dynein; IDA, inner dynein arm; ODA, outer dynein arm; RS, radial spoke. (Scale bar: 10 nm [in *E*, valid also for *A*, *B*, and *D*], 10 nm [in *F*, valid also for *C*].)

Moreover, an N-terminally BCCP-tagged DRC5 construct was poorly expressed and could not be localized (14).

To address the uncertainty about the locations of the N-termini of DRC4 and DRC5, and the C terminus of DRC5, we generated different SNAP- or BCCP-tagged constructs of *DRC4* and *DRC5* and used them to rescue the corresponding mutants *drc4 (pf2)* and *drc5 (sup-pf4)* (Fig. 6 and *SI Appendix*, Figs. S3–S5). The forwarding swimming speeds of the rescued strains, i.e., *pf2-4;N-SNAP-DRC4*, *sup-pf4;DRC5-C-SNAP*, and *sup-pf4;N-BCCP-DRC5*, were significantly faster than the mutants and increased to near WT levels (Fig. 6*B* and *SI Appendix*, Fig. S5*B*). Western blots of purified axonemes demonstrated that the tagged proteins were expressed at endogenous levels and migrated at the sizes predicted for SNAP- or BCCP-tagged DRC subunits (Fig. 6 *C* and *D* and *SI Appendix*, Fig. S5*C*). The SNAP-DRC4 rescue also restored the assembly of other DRC subunits (Fig. 6*C*) that were previously shown to be missing in *pf2* mutant axonemes (13).

Analyses of axonemes from the rescued strains by cryo-ET and subtomogram averaging revealed that the defects in N-DRC structure were completely rescued to WT structure and that the small SNAP and BCCP tags did not interfere with the proper assembly of the N-DRC or other axonemal structures (e.g., compare *SI Appendix*, Fig. S6 *D–F* with *SI Appendix*, Fig. S6 *J–L*). After enhancing the visibility of the cloned tags in the rescued axonemes with streptavidin-nanogold labels, we were able to detect additional densities in the averages of the *SNAP-DRC4* and *DRC5-SNAP* axonemes (Fig. 7, *SI Appendix*, Figs. S3 and S4, and Movies S4 and S5), but not in the *BCCP-DRC5* averages (*SI Appendix*, Fig. S5 *J–L*). The failure to visualize the N terminus of DRC5 is similar to previously reported results (14). However, a clear density corresponding to the labeled N terminus of DRC4 was found on the proximal side of the proximal lobe close to the neighboring B-tubule in *SNAP-DRC4* axonemes (Fig. 7 *D–F*, *SI Appendix*, Fig. S3, and Movie S4). Taken together with the previously determined location of the C terminus of DRC4, our data demonstrate that the DRC4 stretches along the entire length of the N-DRC, i.e., from its attachment site on the A-tubule near the inner DMT junction through the base plate to the proximal lobe. This is a similar structural arrangement to DRC1 and DRC2. The results reveal that DRC4 likely serves both as an anchor that attaches the N-DRC to the A-tubule and as a scaffold for the assembly of the other N-DRC subunits, similar to DRC1 and DRC2. Furthermore, averages of gold-labeled, *DRC5-SNAP* axonemes clearly showed the additional density of the gold nanoparticles that revealed the location of the DRC5 C terminus at the center of the linker close to where the proximal lobe emerges from the linker (Fig. 7 *G–I*, *SI Appendix*, Fig. S4, and Movie S5). Together with previous studies, our data provide a better understanding of the molecular organization of the N-DRC.

Discussion

Analysis by 2D gel electrophoresis, immunoprecipitation, iTRAQ labeling, and mass spectrometry has identified at least 11 N-DRC subunits (12, 13). In this study, by comparing the missing densities

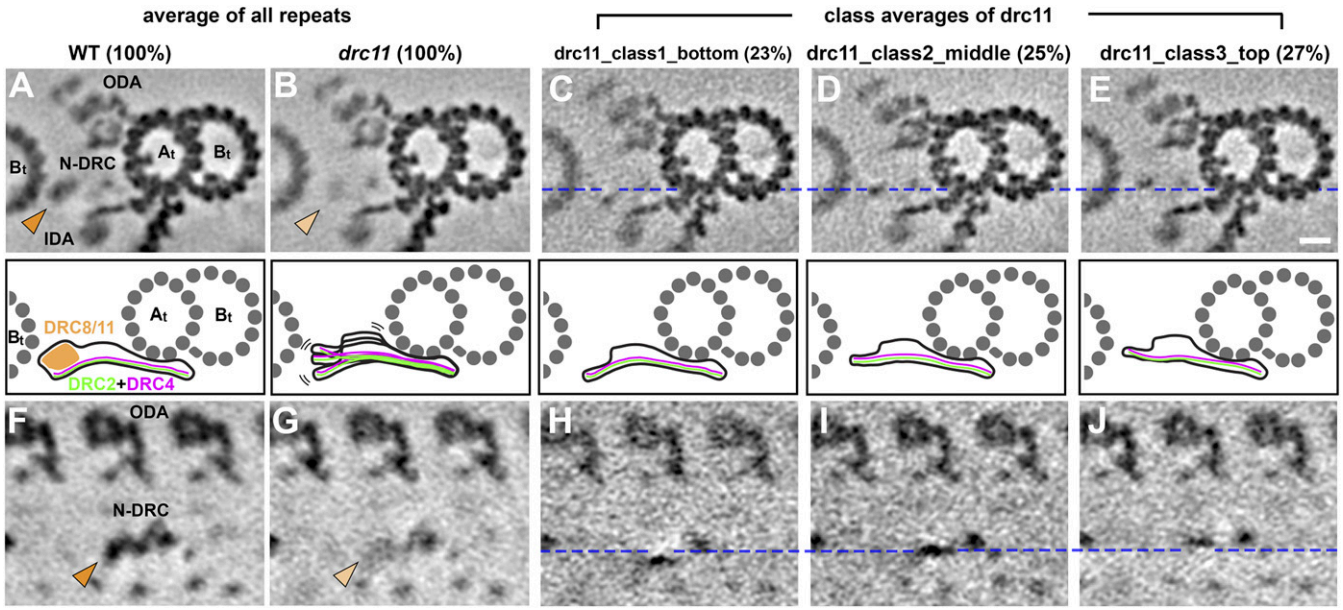

Fig. 5. Classification analyses reveal that the DRC8/11 subcomplex is important for the stability/rigidity of the proximal lobe scaffold (DRC2/4). (*A–J*) Tomographic slices show the averaged axonemal repeats from WT (*A* and *F*) and *drc11* (*B–E* and *G–J*) in cross-sectional (*A–E*) and longitudinal front (*F–J*) views. The first 2 columns show averages of all repeats (100%), whereas columns 3 to 5 show 3 classes of the *drc11* nexin–dynein regulatory complex (N-DRC) that vary in the positions of the proximal lobe (arrowheads). Note the relatively weak and blurry cryo-ET densities of the proximal lobe of the N-DRC in the average-all of *drc11* (light orange arrowheads in *B* and *G*). Classification analysis of this weak density in *drc11* revealed different positions occupied by the proximal lobe (percentages of repeats are indicated for each class); blue dashed lines at the "middle height" serve as reference for the cross-sectional (*C–E*) and longitudinal front (*H–J*) views. Other labels: A_t, A-tubule; B_t, B-tubule; IDA, inner dynein arm; ODA, outer dynein arm. (Scale bar: 10 nm.)

in the subtomogram averages of 2 recently isolated *n-drc* mutants, we have revealed the location of 3 DRC subunits: DRC7 in the linker region including the OID linker, and DRC8/11 in the upper portion of the proximal lobe. We also used gold labeling to determine the precise locations of the N terminus of DRC4 and the C terminus of DRC5 (Table 1). Combined with previous studies (7, 14, 16), we propose a revised model for the overall architecture of the N-DRC: The subunits DRC1, DRC2, and DRC4 form the core scaffold of the N-DRC and a platform for the assembly of functional subunits, including DRC3, DRC5, DRC6, DRC7, DRC8, and DRC11, with this backbone (Fig. 8 and Movie S6).

DRC1, DRC2, and DRC4 Form the Backbone of the N-DRC. Cryo-ET and subtomogram averages of the axonemal repeat from *Chlamydomonas* null mutants of *drc1* (*pf3*), *drc2* (*ida6*), and *drc4* (*pf2*) previously revealed large-scale defects in the structure of the N-DRC, i.e., missing or reduced densities in both the base plate and the linker domains (7, 16, 23). Transformation with WT or tagged versions of DRC1, DRC2, or DRC4 fully restored the missing polypeptides and structures (7, 14, 16). The localization of the termini of DRC1, DRC2, and DRC4 in the previous and current studies suggests that all 3 subunits stretch along the entire N-DRC, i.e., from the inner junction to the neighboring DMT (14, 16). In addition, the use of advanced microscope hardware, such as a direct electron detector camera and Volta-Phase-Plate, has increased the resolution of our subtomogram averages, allowing us to visualize 3 filamentous structures in the base plate that are slightly twisted around each other like a rope (Fig. 8*C*). This is consistent with the high-resolution reconstruction of the WT *Tetrahymena* N-DRC using our recently developed TYGRESS software (26). These findings suggest that DRC1, DRC2, and DRC4 function as scaffold and play a pivotal role in the assembly of the entire N-DRC structure. Among the 3 backbone proteins, the subcomplex of DRC1 and DRC2 is the most critical as its absence in the *pf3* (*drc1*) and *ida6* (*drc2*) mutants caused reduced densities for the entire N-DRC base plate, including DRC4 (16, 23). Thus, DRC1 and DRC2 form likely the core filament at the very bottom of the N-DRC base plate, which directly associates with the A-tubule (Fig. 8*C*, yellow and dark green). DRC4 does not appear to be necessary for assembly of DRC1 and DRC2 into the base plate, as the *pf2* mutant has substantial remaining base-plate density, suggesting that DRC4 likely forms the filamentous structure on top of the DRC1/DRC2 subcomplex in the N-DRC base plate (Fig. 8*C*, purple) (16, 23).

All scaffold components (DRC1, DRC2, and DRC4) are highly conserved in motile cilia and flagella, from unicellular algae *Chlamydomonas* to human. Genetic studies of the orthologs in different species have revealed that DRC1, DRC2, and DRC4 play essential and conserved roles in ciliary and flagellar motility. For example, an insertion into the *DRC4* locus in *Chlamydomonas* resulted in an altered ciliary waveform and slow swimming cells of the *pf2* strain (22). RNA interference-mediated knockdown of the *DRC4* ortholog in trypanosomes revealed that DRC4 is required for flagellar motility and is essential for the viability of the bloodstream form of the parasite (27). The vertebrate orthologs of DRC4 are GAS11 in human and GAS8 in mice and zebrafish, and mutations in *GAS11* cause primary ciliary dyskinesia (28).

Previous cryo-ET studies failed to unambiguously identify the location of the N terminus of DRC4. Oda et al. (14) reported that the labeling density of the N terminus of DRC4 appeared to be present in 2 locations, with one density at the proximal lobe and the other at the distal lobe. In contrast, in our studies, the SNAP-tagged density clearly localized the N terminus of DRC4 at the proximal lobe (Fig. 7 *D–F*). The 96-nm averaged repeats of the *drc11* mutant showed a density that remains at the bottom (IDA-facing side) of the proximal lobe (Fig. 5). These results suggest that the N-terminal parts of DRC2 and DRC4 form the structural scaffold at the bottom of the proximal lobe, which can bind to the DRC8/11 subcomplex.

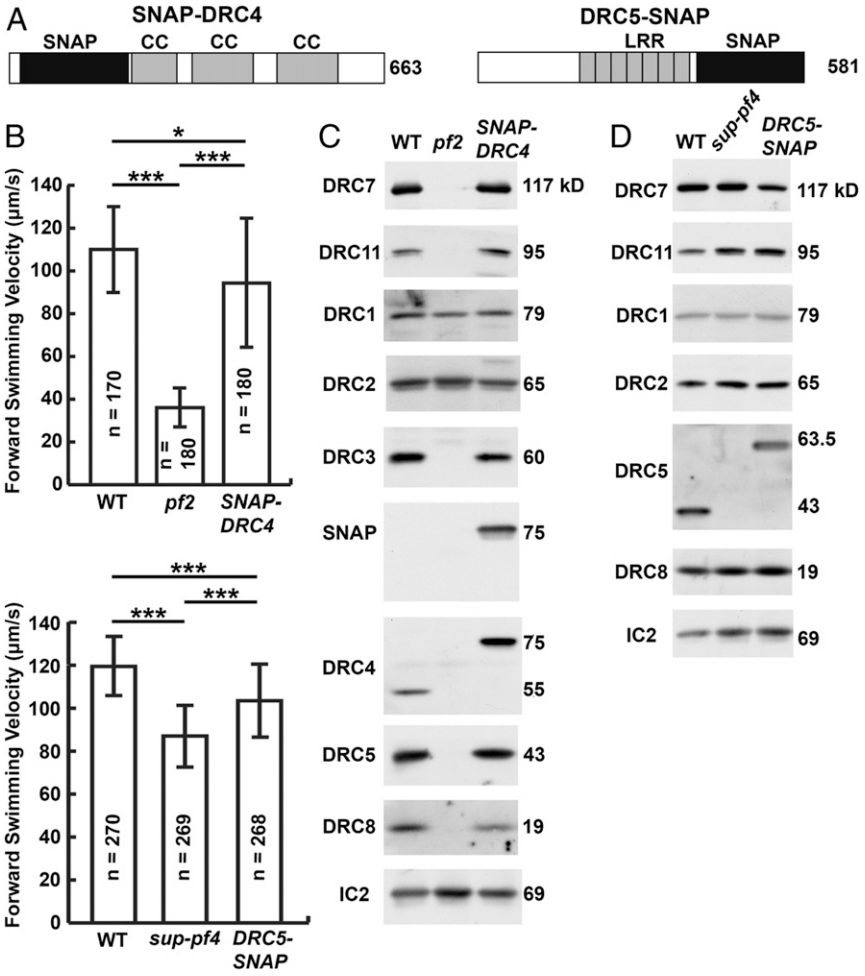

Fig. 6. Rescue of *drc4 (pf2)* and *drc5 (sup-pf4)* mutants by transformation with SNAP-tagged DRC subunits. (*A*) The DRC4 and DRC5 protein sequences are drawn to scale, with the location of predicted polypeptide domains indicated: CC, coiled-coil domain; LRR, leucine-rich repeat; SNAP, SNAP tags introduced near the N terminus of DRC4 and the C terminus of DRC5. (*B*) The forward swimming velocities of *drc* mutants as measured by phase contrast microscopy are shown relative to those of wild-type (WT) and rescued strains generated by transformation with the indicated SNAP-tagged *DRC* gene. As indicated by the asterisks (*$P < 0.05$; ***$P < 0.001$), both *drc* mutants were significantly slower than WT and the SNAP-tagged rescue strains, but the latter were also slightly slower than WT. (*C* and *D*) Western blots of axonemes isolated from WT, *drc* mutants, and SNAP-tagged rescued strains were probed with antibodies against several DRC subunits. Note the presence of bands that migrated at the sizes predicted for SNAP-tagged DRC subunits. An antibody against the IC2 subunit of the outer dynein arms served as a loading control.

DRC3, 5, 6, 7, 8, and 11 Are Attached to the N-DRC Backbone and Interact with Other Axonemal Complexes. Loss of DRC3 (*drc3*), DRC5/DRC6 (*sup-pf4*), DRC7 (*drc7*), and DRC8/DRC11 (*drc11*) cause defects in certain regions of the N-DRC but have minimal effects on the assembly of other DRC subunits, unlike loss of the backbone subunits (7, 15, 16).

DRC5 is a leucine-rich repeat (LRR) protein that appears to be closely associated with DRC6 based on the absence of DRC6 in the DRC5 mutant *sup-pf4* (12, 29). Cryo-ET and subtomogram averaging revealed that the L2 protrusion of N-DRC linker, which is located in front of the OID linker, is missing in *sup-pf4* axonemes (7) (*SI Appendix*, Fig. S6 *G* and *I*). The motility defects observed in the *Chlamydomonas sup-pf4* mutant are subtle. The *sup-pf4* mutant and the tubulin polyglutamylation (*tpg1*) mutant can both undergo reactivated motility in the presence of ATP, like WT cells, whereas the *sup-pf4;tpg1* double mutant failed to reactivate motility in the presence of ATP. In addition, *sup-pf4;tpg1* axonemes were more prone to splaying, i.e., the 9 DMTs separated more easily from each other, suggesting that DRC5/6 and B-tubule glutamylation of the neighboring DMT work together to maintain axonemal integrity and ciliary motility (30). However, it is not known which DRC subunit(s) make direct contact with the neighboring B-tubule. Here, cryo-ET localization of a tagged rescue strain suggested that the C terminus of DRC5 is located in the center of the N-DRC linker domain, rather than close to the neighboring DMT. The N-terminal tag of BCCP-DRC5 could not be visualized (*SI Appendix*, Fig. S5 *J–L*), even though Western blots of the rescued strain clearly showed that BCCP-DRC5 was expressed at WT levels (*SI Appendix*, Fig. S5*C*), indicating that the addition of the BCCP tag does not interfere with the incorporation of DRC5 into N-DRC. Two possible reasons for failing to detect the location of the N terminus of DRC5 might be that it is buried so deep in the structure of the N-DRC that the streptavidin-gold could not bind to the tag or that the N-terminal domain may be so flexible in position that the gold density would be averaged out in the subtomogram averages.

DRC7 is the largest N-DRC subunit (177 kDa) identified in *Chlamydomonas*. It contains a highly conserved transglutaminase-like (TGL) peptidase domain, which is predicted to bind tightly to glutamylated proteins, suggesting DRC7 may interact with glutamylated residues on the neighboring B-tubule (13). This idea is supported by our cryo-ET and subtomogram averaging images that show that a part of the distal lobe is missing in the *drc7* axonemes. However, the major defect in the *drc7* axonemes was seen in the middle segment of the N-DRC linker, including a missing OID linker that usually connects the N-DRC to the ODA row. The OID linker is proposed to be part of the signal transduction pathway that regulates ciliary beating: Signals are transferred from the CPC to the RS, then to the N-DRC and I1 dynein, finally reaching the ODAs via 2 routes; one OID linker from the N-DRC and a second OID linker from the I1 intermediate/light-chain complex, respectively (31–33). However, even though the defects in N-DRC structure seem to disrupt 2 important interfaces with neighboring structures, *drc7* mutant did not show significant defects in forward swimming velocity under standard culture conditions in *Chlamydomonas*. A possible explanation for the lack of a strong motility phenotype in *Chlamydomonas drc7* mutants might be that there are other—(partially) redundant—pathways for

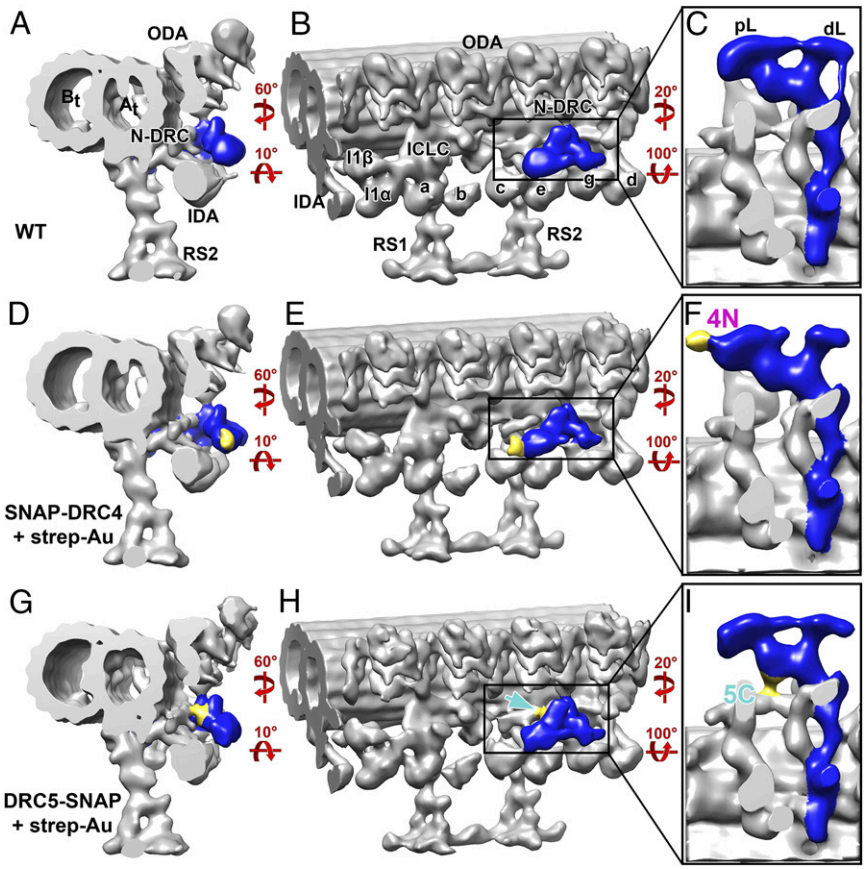

Fig. 7. Precise localization of the N terminus of DRC4, and the C terminus of DRC5 by SNAP tag labeling and cryo-ET. Three-dimensional isosurface renderings show the structures of the 96-nm repeats in WT (*A–C*), labeled *SNAP-DRC4* (*D–F*), and labeled *DRC5-SNAP* (*G–I*) axonemes after cryo-ET and subtomogram averaging. Purified axonemes with SNAP-tagged DRC4 (*D–F*) or DRC5 (*G–I*) were labeled with streptavidin-Au (1.4-nm nanogold). Cross-sectional (*A*, *D*, and *G*), longitudinal front (*B*, *E*, and *H*), and enlarged longitudinal bottom views (*C*, *F*, and *I*; looking from the axoneme center outward) of the nexin–dynein regulatory complex (N-DRC, blue) show the additional density of the SNAP-biotin-strep-Au label (manually colored gold): at the proximal lobe (pL) of the N-DRC linker in the N-terminally labeled DRC4 axonemes (*D–F*), and at the center of the N-DRC linker in the C-terminally labeled DRC5 axonemes (*G–I*). Other labels: a–e and g, inner dynein arm isoforms; A_t, A-tubule; B_t, B-tubule; dL, distal lobe; I1α/I1β/ICLC, α- and β-heavy chain, and intermediate/light-chain complex of I1 dynein; IDA, inner dynein arm; ODA, outer dynein arm; RS, radial spoke.

signal transduction. The N-DRC connects to the neighboring B-tubule via both the proximal and distal lobes, and the loss of the distal lobe in the *drc7* mutant might be compensated for by the remaining proximal lobe that still interacts with the neighboring B-tubule. In addition to the OID linker from the N-DRC, also the I1 ICLC connects between the RS/IDA row to the ODAs, and these 2 signal transduction pathways between the IDA and ODA rows might be redundant for the activity control of the ODAs. Future study of double mutants in *Chlamydomonas* may reveal a more profound effect of the *drc7* mutation. Another possibility is that DRC7 might be critical for motility under more stringent conditions. In *Drosophila*, loss of the *DRC7* ortholog *CG34110* (*lost boys*, *lobo)* causes defects in sperm storage and fertility (34). Future studies will have to clarify the reasons for this more severe phenotype in flies, but a recent survey of motility genes expressed in *Drosophila* sperm has revealed that not all DRC subunits are expressed in the testis (35). Thus, it is also possible that loss of DRC7 may cause a more significant functional defects in other species.

DRC8 contains an EF-hand domain (a calcium-binding helix–loop–helix structural motif) that could bind Ca^{2+}, and DRC11 contains a calmodulin-binding motif, suggesting these 2 subunits may contribute to the calcium regulation of flagellar motility. DRC11 also contains an "ATPases associated with diverse cellular activities" (AAA) domain that could mediate nucleotide-sensitive conformational changes. Our studies of the *drc11* mutant showed that DRC11 is required for the assembly of DRC8, and DRC8/11 probably form a subcomplex localized to the proximal lobe of the linker domain that contacts the neighboring B-tubule (Fig. 4). Thus, we propose that the DRC8/11 subunits regulate cilia motility by modulating contacts with the neighboring B-tubule, which could be important for transforming interdoublet sliding to ciliary bending, and/or provide signal feedback. The ortholog CMF22 in *Trypanosoma brucei* is required for normal flagellar beating patterns and propulsive cell motility (36). However, in *Chlamydomonas*, we only observed small decreases in the swimming velocity of the *drc11* mutant compared to WT cells (Fig. 2*B*). One possible explanation may be that the N-DRC connects to the neighboring B-tubule via both the proximal lobe and the distal lobe. The proximal lobe is missing in the *drc11* mutant, but the remaining distal lobe could interact with the B-tubule and transform the interdoublet sliding to bending.

Orthologs of N-DRC subunits have been found in motile cilia, both "9 + 2" and "9 + 0" of many species (13, 37, 38), but not in nonmotile primary 9 + 0 cilia (39, 40). The fact that the N-DRC seems to be present in all motile cilia, even in motile 9 + 0 cilia that can lack almost any other major axonemal complexes, such as the CPC, RSs, and IDAs or ODAs (6, 37), suggests an essential and central role for the N-DRC in regulating ciliary motility. Our results provide insights into several important aspects of N-DRC assembly and function, from revealing the precise location of several DRC subunits, the overall organization of the N-DRC with a 3-subunit core-complex (DRC1/2/4) that serves as the scaffold for the assembly of the "functional subunits" (DRC3/5–8/11), shedding light on the molecular mechanism by which the N-DRC regulates dynein activity and thus flagellar beating.

Methods

Culture Conditions, Strain Construction, and Identification of Recently Isolated Mutations. Strains, including WT *Chlamydomonas reinhardtii* and CLiP mutants (*SI Appendix*, Table S1), and mutant strains rescued with tagged DRC subunits were cultured as previously described (13) (see *SI Appendix* for more details on the identification and characterization of *drc* mutants and the construction of epitope-tagged *N-DRC* strains). The *Chlamydomonas*

Table 1. Summary of polypeptides and structures present or absent in the strains used in this study

Components	Strains							
	WT	*drc7*	*drc11*	*pf2*	*SNAP-DRC4*	*sup-pf-4*	*DRC5-SNAP*	*BCCP-DRC5*
Polypeptides (kDa)								
DRC1 (79)	+	+	+	+	+	+	+	+
DRC2 (65)	+	+	+	+	+	+	+	+
DRC3 (60)	+	+	+	–	+	+	+	+
DRC4 (55)	+	+	+	–	+	+	+	+
DRC5 (43)	+	+	+	–	+	–	+	+
DRC6 (28)	+	+	+	–	+	–	+	+
DRC7 (177)	+	–	+	–	+	+	+	+
DRC8 (19)	+	+	–	–	+	+	+	+
DRC9 (46)	+	+	+	–	+	+	+	+
DRC10 (41)	+	+	+	–	+	+	+	+
DRC11 (95)	+	+	–	–	+	+	+	+
Structure (kDa)								
Base plate (~300)	+	+	+	+/–	+	+	+	+
Linker								
Proximal lobe (~350)	+	+	–	–	+	+	+	+
Distal lobe (~100)	+	+/–	+	–	+	+/–	+	+
L2 protrusion (~200)	+	+	+	–	+	–	+	+
OID linker (~200)	+	–	+	–	+	+	+	+

+ indicates that the component was present at WT levels; – indicates that the component was absent; +/– indicates that the component was present at reduced levels. Molecular mass of the N-DRC structure is estimated from the isosurface rendering and indicated in parentheses (in kilodaltons).

strain *cw15*, which was used as the background strain for the CLiP library, is cell wall-less but assembles flagella resembling those of WT (*cc-125*).

Phase Contrast, Fluorescence Microscopy, and Measurements of Swimming Velocity. Transformants and candidate *drc* mutants were screened by phase contrast microscopy using a 20× or 40× objective, a halogen light source, and a red filter on a Zeiss Axioskop. Forward swimming velocities were measured using a Rolera-MGi EM-CCD camera (Q Imaging) and the Metamorph software package, version 7.6.5.0 (Molecular Devices), as previously described (13). The forward swimming velocities of the CLiP mutants and CLiP-mutant rescues were compared with the "WT"-like CLiP background strain *cw15*, whereas *pf2*, *suppf4*, *SNAP-DRC4*, *DRC5-SNAP*, and *BCCP-SNAP* were compared to the WT strain *cc-125*. Some transformants were screened for the presence of the SNAP or BCCP tag by immunofluorescence microscopy (41).

Preparation of Purified Axonemes for SDS/PAGE, Western Blotting, iTRAQ Labeling, and Mass Spectrometry. *Chlamydomonas* isolated axonemes were prepared as previously described (13, 42). Briefly, *Chlamydomonas* cells were collected by centrifugation and resuspended in pH shock buffer containing

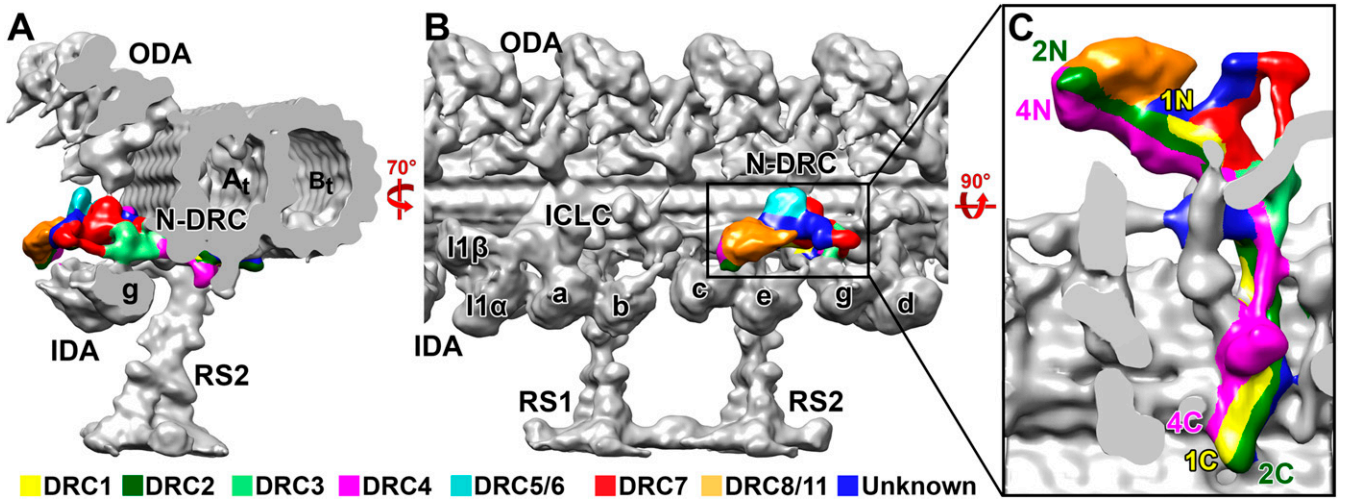

Fig. 8. Updated model of the DRC subunit organization and N-DRC interactions with neighboring structures. The locations of the DRC subunits are summarized and colored in the WT nexin–dynein regulatory complex (N-DRC) structure, which is shown in cross-sectional (*A*), longitudinal front (*B*), and enlarged bottom (*C*) views. The structural comparison between the averaged WT axonemal repeat and deletion mutants of DRC subunits or mutant rescues by tagged DRC subunits revealed the architecture of the N-DRC: The core scaffold extends along the entire length of the N-DRC and consists of DRC1 (yellow), DRC2 (dark green), and DRC4 (magenta); with this scaffold associate several functional subunits, i.e., DRC3 (light green), DRC5/6 subcomplex (cyan), DRC7 (red), and DRC8/11 subcomplex (orange). The composition of a few areas within the N-DRC remain unknown (dark blue). Other labels: a–e and g, inner dynein arm isoforms; A_t, A-tubule; B_t, B-tubule; I1α/I1β/ICLC, α- and β-heavy chain, and intermediate/light-chain complex of I1 dynein; IDA, inner dynein arm; ODA, outer dynein arm; RS, radial spoke.

10 mM Hepes, pH 7.4, 1 mM $SrCl_2$, 4% sucrose, and 1 mM DTT. Flagella were detached from cells by adding 0.5 M acetic acid to reduce the pH to 4.3. After 80 s, the pH was increased to 7.4 by adding 1 M KOH. The flagella pellets were then demembranated by adding 1% Igepal CA 630 (Sigma-Aldrich) to the solution with gentle rotation for 20 min at 4 °C. Axonemes were collected by centrifugation at 10,000 × *g* for 10 min and resuspended in HMEEN (10 mM Hepes, 5 mM $MgSO_4$, 1 mM EGTA, 0.1 mM EDTA, 30 mM NaCl, pH 7.4) plus 1 mM DTT and 0.1 μg/mL protease inhibitors (leupeptin, aprotinin, and pepstatin). Samples were separated on 5 to 15% polyacrylamide gradient gels, transferred to Immobilon P, and probed with the different antibodies listed in *SI Appendix*, Table S8, as described by ref. 13.

For iTRAQ labeling and mass spectrometry, isolated axonemes were washed with 10 mM Hepes, pH 7.4, to remove salt, DTT, and protease inhibitors, and then resuspended in 0.5 M triethylammonium bicarbonate, pH 8.5, and processed for trypsin digestion and iTRAQ labeling as described in refs. 13 and 41. Samples were combined and fractionated off-line using high pH, C18 reversed-phase chromatography. Column fractions were vacuumed dried, resuspended in solvent (98:2:0.01, water/acetonitrile/formic acid), and loaded in 1- to 1.5-μg aliquots for capillary LC using a C18 column at low pH. The C18 column was mounted in a nanospray source directly in line with a Velos Orbitrap mass spectrometer (Thermo Fisher Scientific). On-line capillary LC, MS/MS, database searching, and protein identification were performed as previously described (13, 43) using ProteinPilot software, version 5.0 (AB Sciex), and the most recent version (version 5.5) of the *Chlamydomonas* database (https://phytozome.jgi.doe.gov/pz/portal.html). The bias factors for all samples were normalized to α- and β-tubulin.

WT (*cw15*) and *drc* axonemes were each labeled with 2 different iTRAQ reagents in a 4-plex experiment (technical replicates), and then each 4-plex experiment was repeated with new samples (biological replicates). For the *drc7* (197909) mutant, 1,166 proteins were detected with high confidence at a false-discovery rate of 5% in the first 4-plex experiment, and 701 proteins were detected in the second experiment. For the *drc11* (068819) mutant, 949 proteins were detected in the first 4-plex experiment, and 768 proteins were detected in the second experiment. The datasets were further filtered to identify those proteins that were identified by at least 5 peptides and whose mutant/WT ratios were significantly different ($P < 0.05$) from WT/WT in all replicates.

Axoneme Preparation and SNAP-Gold Labeling for Cryo-ET. *Chlamydomonas* axonemes for cryo-ET were prepared as mentioned above. The only difference is that the final axoneme pellets were resuspended in HMEEK buffer (30 mM Hepes, 5 mM $MgSO_4$, 1 mM EGTA, 0.1 mM EDTA, and 25 mM KCl, pH 7.4). A volume of 3 μL of the isolated axonemes was added to glow-discharged R2/2 holey carbon-coated grids and gently mixed with 1 μL of 10-times-concentrated, BSA-coated 10-nm gold solution (44). After ∼2 s of backside blotting with filter paper, the grid was rapidly plunge frozen in liquid ethane with a homemade plunge freezer. Frozen grids were stored in liquid nitrogen until used.

For SNAP-gold labeling samples, the SNAP tag was labeled with gold as previously described (16). Briefly, 1 μL of 1 mM BG-biotin or BG-$(PEG)_{12}$-biotin (New England Biolabs; PEG linker available on request) was added to 200 μL of the purified axonemes in HMEEK buffer and incubated overnight at 4 °C. Unbound BG substrate was removed by centrifugation at 10,000 × *g* for 10 min at 4 °C and 3 wash steps with HMEEK buffer. The axoneme pellet was resuspended in 200 μL of HMEEK buffer. After adding 5 μL of 80 μg/mL 1.4-nm-sized streptavidin nanogold particles (strep-Au; Nanoprobes), the suspension was incubated at 4 °C for 4 h. After adding 800 μL of HMEEK buffer, the labeled axonemes were pelleted by centrifugation at 10,000 × *g* for 10 min at 4 °C and resuspended in 200 μL of HMEEK buffer.

Cryo-ET. Vitrified grids were imaged using a Titan Krios transmission electron microscope (used for all samples unless otherwise noted) or Tecnai F30 (used for WT, *SNAP-DRC4*, *DRC5-SNAP*, and *BCCP-DRC5* axonemes) both operated at 300 kV. Images were captured using a 4k × 4k K2 direct detection camera (Gatan) on the Titan Krios at a magnification of 26,000× (yielding a scaling of 5.5 Å per pixel) or a 2k × 2k charge-coupled device camera (Gatan) on the Tecnai F30 at a magnification of 13,500× (yielding a scaling of 10.0 Å per pixel). Tilt series were collected from 60° to −60° in 2° steps using dose-symmetric method on the Titan Krios. Counting mode of the K2 camera was used and for each tilt image 15 frames (0.4-s exposure time for each frame) were recorded. Both cameras were placed behind a postcolumn energy filter (Gatan) that was operated in zero-loss mode (20-eV slit width). Data acquisition was performed using the microscope control software SerialEM (45) in low-dose mode, and the total electron dose per tilt series was limited to ∼100 e/Å^2.

Image Processing. The frames of each tilt series image collected on a K2 camera were aligned and then merged using the script extracted from the IMOD software package (46) to generate the final tilt serial dataset. Tomograms were reconstructed using fiducial alignment and the back-projection method in the IMOD package (46). Subtomogram averaging was performed using the PEET software (19, 20) to average the 96-nm axonemal repeat units from 3D reconstructed axonemes. The resolution of the DMT averages was estimated using the 0.5 criterion of the Fourier shell correlation method (*SI Appendix*, Table S5). The Chimera package (47) was used for 3D visualization and surface rendering. Mass estimations of the DRC complex and subvolumes were calculated using the average density of 1.43 g/cm^3 for proteins (48) and after normalizing the isosurface-rendering threshold to the mass of MTs.

For the classification of the lower proximal lobe of the N-DRC linker, a cylindrical mask (size, 12 × 12 × 16 pixels) was placed over the area containing the lower proximal lobe to "hide" everything except this area of interest. Focusing on this area, we then performed a principal-component analysis of the aligned subtomogram volumes (axonemal repeats) from WT and *drc11* (20); 15 features were selected for clustering, generating 12 subclasses that were then partially combined into 3 distinct classes based on the position of the remaining proximal lobe between the rows of the inner and outer dynein arms.

Data Availability. The averaged structures reported in this paper have been deposited in the Electron Microscopy Data Bank under accession codes EMD-20338 (49), EMD-20339 (50), EMD-20340 (51), EMD-20341 (52), and EMD-20821 (53).

ACKNOWLEDGMENTS. We thank Chen Xu (Brandeis University) and Zhenguo Chen and Daniel Stoddard (University of Texas [UT] Southwestern Medical Center) for management of the electron microscope facilities and training. The UT Southwestern Cryo-Electron Microscopy Facility is supported in part by Cancer Prevention and Research Institute of Texas (CPRIT) Core Facility Support Award RP170644. We also thank Gang Fu for assisting with tomogram reconstruction. We are grateful to Cai Kai for critical reading of the manuscript. We also thank LeeAnn Higgins and Todd Markowski in the Center for Mass Spectrometry and Proteomics at the University of Minnesota for assistance with mass spectrometry of the iTRAQ-labeled samples. This center is supported by multiple grants including National Science Foundation (NSF) Major Research Instrumentation Grants 9871237 and NSF-DBI-0215759 as described at https://cbs.umn.edu/cmsp/about. We also acknowledge Matt Laudon and the *Chlamydomonas* Genetics Center (University of Minnesota) for strains. This facility is supported by the NSF Living Stock Collections for Biological Research Program Grants 0951671 and 00017383. The antibody to RSP16 was generously provided by Pinfen Yang (Marquette University) and the antibody to DRC1 by Win Sale (Emory University). This study was funded by the following grants: National Institutes of Health Grants R01GM083122 (to D.N.) and R01GM055667 (to M.E.P.), and CPRIT Grant RR140082 (to D.N.).

1. M. Fliegauf, T. Benzing, H. Omran, When cilia go bad: Cilia defects and ciliopathies. *Nat. Rev. Mol. Cell Biol.* **8**, 880–893 (2007).
2. H. M. Mitchison, E. M. Valente, Motile and non-motile cilia in human pathology: From function to phenotypes. *J. Pathol.* **241**, 294–309 (2017).
3. N. Mizuno, M. Taschner, B. D. Engel, E. Lorentzen, Structural studies of ciliary components. *J. Mol. Biol.* **422**, 163–180 (2012).
4. P. Satir, Studies on cilia. 3. Further studies on the cilium tip and a "sliding filament" model of ciliary motility. *J. Cell Biol.* **39**, 77–94 (1968).
5. K. E. Summers, I. R. Gibbons, Adenosine triphosphate-induced sliding of tubules in trypsin-treated flagella of sea-urchin sperm. *Proc. Natl. Acad. Sci. U.S.A.* **68**, 3092–3096 (1971).
6. D. M. Woolley, Studies on the eel sperm flagellum. I. The structure of the inner dynein arm complex. *J. Cell Sci.* **110**, 85–94 (1997).
7. T. Heuser, M. Raytchev, J. Krell, M. E. Porter, D. Nicastro, The dynein regulatory complex is the nexin link and a major regulatory node in cilia and flagella. *J. Cell Biol.* **187**, 921–933 (2009).
8. M. Kikkawa, Big steps toward understanding dynein. *J. Cell Biol.* **202**, 15–23 (2013).
9. A. J. Roberts, T. Kon, P. J. Knight, K. Sutoh, S. A. Burgess, Functions and mechanics of dynein motor proteins. *Nat. Rev. Mol. Cell Biol.* **14**, 713–726 (2013).
10. J. Lin, D. Nicastro, Asymmetric distribution and spatial switching of dynein activity generates ciliary motility. *Science* **360**, eaar1968 (2018).

11. R. Viswanadha, W. S. Sale, M. E. Porter, Ciliary motility: Regulation of axonemal dynein motors. *Cold Spring Harb. Perspect. Biol.* **9**, a018325 (2017).
12. J. Lin *et al*., Building blocks of the nexin-dynein regulatory complex in *Chlamydomonas* flagella. *J. Biol. Chem.* **286**, 29175–29191 (2011).
13. R. Bower *et al*., The N-DRC forms a conserved biochemical complex that maintains outer doublet alignment and limits microtubule sliding in motile axonemes. *Mol. Biol. Cell* **24**, 1134–1152 (2013).
14. T. Oda, H. Yanagisawa, M. Kikkawa, Detailed structural and biochemical characterization of the nexin-dynein regulatory complex. *Mol. Biol. Cell* **26**, 294–304 (2015).
15. J. Awata *et al*., DRC3 connects the N-DRC to dynein g to regulate flagellar waveform. *Mol. Biol. Cell* **26**, 2788–2800 (2015).
16. K. Song *et al*., *In situ* localization of N and C termini of subunits of the flagellar nexin-dynein regulatory complex (N-DRC) using SNAP tag and cryo-electron tomography. *J. Biol. Chem.* **290**, 5341–5353 (2015).
17. X. Li *et al*., An indexed, mapped mutant library enables reverse genetics studies of biological processes in *Chlamydomonas reinhardtii*. *Plant Cell* **28**, 367–387 (2016).
18. X. Li *et al*., A genome-wide algal mutant library and functional screen identifies genes required for eukaryotic photosynthesis. *Nat. Genet.* **51**, 627–635 (2019).
19. D. Nicastro *et al*., The molecular architecture of axonemes revealed by cryoelectron tomography. *Science* **313**, 944–948 (2006).
20. J. M. Heumann, A. Hoenger, D. N. Mastronarde, Clustering and variance maps for cryo-electron tomography using wedge-masked differences. *J. Struct. Biol.* **175**, 288–299 (2011).
21. V. Lučić, F. Förster, W. Baumeister, Structural studies by electron tomography: From cells to molecules. *Annu. Rev. Biochem.* **74**, 833–865 (2005).
22. G. Rupp, M. E. Porter, A subunit of the dynein regulatory complex in *Chlamydomonas* is a homologue of a growth arrest-specific gene product. *J. Cell Biol.* **162**, 47–57 (2003).
23. R. Bower *et al*., DRC2/CCDC65 is a central hub for assembly of the nexin-dynein regulatory complex and other regulators of ciliary and flagellar motility. *Mol. Biol. Cell* **29**, 137–153 (2018).
24. C. Austin-Tse *et al*., Zebrafish ciliopathy screen plus human mutational analysis identifies C21orf59 and CCDC65 defects as causing primary ciliary dyskinesia. *Am. J. Hum. Genet.* **93**, 672–686 (2013).
25. M. Wirschell *et al*., The nexin-dynein regulatory complex subunit DRC1 is essential for motile cilia function in algae and humans. *Nat. Genet.* **45**, 262–268 (2013).
26. K. Song *et al*., Structure of the ciliary axoneme at nanometer resolution reconstructed by TYGRESS. *Nat. Methods*, 10.1038/s41592-019-0651-0.
27. K. S. Ralston, K. L. Hill, Trypanin, a component of the flagellar dynein regulatory complex, is essential in bloodstream form African trypanosomes. *PLoS Pathog.* **2**, e101 (2006).
28. H. Olbrich *et al*., Loss-of-function GAS8 mutations cause primary ciliary dyskinesia and disrupt the nexin-dynein regulatory complex. *Am. J. Hum. Genet.* **97**, 546–554 (2015).
29. B. Huang, Z. Ramanis, D. J. Luck, Suppressor mutations in *Chlamydomonas* reveal a regulatory mechanism for flagellar function. *Cell* **28**, 115–124 (1982).
30. L. M. Alford *et al*., The nexin link and B-tubule glutamylation maintain the alignment of outer doublets in the ciliary axoneme. *Cytoskeleton (Hoboken)* **73**, 331–340 (2016).
31. M. E. Porter, W. S. Sale, The 9 + 2 axoneme anchors multiple inner arm dyneins and a network of kinases and phosphatases that control motility. *J. Cell Biol.* **151**, F37–F42 (2000).
32. M. Wirschell *et al*., Regulation of ciliary motility: Conserved protein kinases and phosphatases are targeted and anchored in the ciliary axoneme. *Arch. Biochem. Biophys.* **510**, 93–100 (2011).
33. T. Oda, T. Yagi, H. Yanagisawa, M. Kikkawa, Identification of the outer-inner dynein linker as a hub controller for axonemal dynein activities. *Curr. Biol.* **23**, 656–664 (2013).
34. Y. Yang *et al*., Regulation of flagellar motility by the conserved flagellar protein CG34110/Ccdc135/FAP50. *Mol. Biol. Cell* **22**, 976–987 (2011).
35. P. Zur Lage, F. G. Newton, A. P. Jarman, Survey of the ciliary motility machinery of *Drosophila* sperm and ciliated mechanosensory neurons reveals unexpected cell-type specific variations: A model for motile ciliopathies. *Front. Genet.* **10**, 24 (2019).
36. H. T. Nguyen, J. Sandhu, G. Langousis, K. L. Hill, CMF22 is a broadly conserved axonemal protein and is required for propulsive motility in *Trypanosoma brucei*. *Eukaryot. Cell* **12**, 1202–1213 (2013).
37. E. V. Armbrust *et al*., The genome of the diatom *Thalassiosira pseudonana*: Ecology, evolution, and metabolism. *Science* **306**, 79–86 (2004).
38. W. R. Lewis *et al*., Mutation of growth arrest specific 8 reveals a role in motile cilia function and human disease. *PLoS Genet.* **12**, e1006220 (2016).
39. S. S. Merchant *et al*., The *Chlamydomonas* genome reveals the evolution of key animal and plant functions. *Science* **318**, 245–250 (2007).
40. H. Ishikawa, J. Thompson, J. R. Yates, 3rd, W. F. Marshall, Proteomic analysis of mammalian primary cilia. *Curr. Biol.* **22**, 414–419 (2012).
41. J. Reck *et al*., The role of the dynein light intermediate chain in retrograde IFT and flagellar function in *Chlamydomonas*. *Mol. Biol. Cell* **27**, 2404–2422 (2016).
42. G. B. Witman, Isolation of *Chlamydomonas* flagella and flagellar axonemes. *Methods Enzymol.* **134**, 280–290 (1986).
43. Y. Lin-Moshier *et al*., Re-evaluation of the role of calcium homeostasis endoplasmic reticulum protein (CHERP) in cellular calcium signaling. *J. Biol. Chem.* **288**, 355–367 (2013).
44. C. V. Iancu *et al*., Electron cryotomography sample preparation using the Vitrobot. *Nat. Protoc.* **1**, 2813–2819 (2006).
45. D. N. Mastronarde, Automated electron microscope tomography using robust prediction of specimen movements. *J. Struct. Biol.* **152**, 36–51 (2005).
46. J. R. Kremer, D. N. Mastronarde, J. R. McIntosh, Computer visualization of three-dimensional image data using IMOD. *J. Struct. Biol.* **116**, 71–76 (1996).
47. E. F. Pettersen *et al*., UCSF Chimera—a visualization system for exploratory research and analysis. *J. Comput. Chem.* **25**, 1605–1612 (2004).
48. M. L. Quillin, B. W. Matthews, Accurate calculation of the density of proteins. *Acta Crystallogr. D Biol. Crystallogr.* **56**, 791–794 (2000).
49. L. Gui *et al*., The nexin-dynein regulatory complex (N-DRC) from the cryo-electron tomography and subtomographic average of isolated *Chlamydomonas* wild type axonemes. Electron Microscopy Data Bank. https://www.ebi.ac.uk/pdbe/entry/emdb/EMD-20338. Deposited 25 June 2019.
50. L. Gui *et al*., The nexin-dynein regulatory complex (N-DRC) from the cryo-electron tomography and subtomographic average of isolated *Chlamydomonas* drc7 axonemes. Electron Microscopy Data Bank. https://www.ebi.ac.uk/pdbe/entry/emdb/EMD-20339. Deposited 25 June 2019.
51. L. Gui *et al*., The nexin-dynein regulatory complex (N-DRC) from the cryo-electron tomography and subtomographic average of isolated *Chlamydomonas* drc11 axonemes. Electron Microscopy Data Bank. https://www.ebi.ac.uk/pdbe/entry/emdb/EMD-20340. Deposited 25 June 2019.
52. L. Gui *et al*., The nexin-dynein regulatory complex (N-DRC) from the cryo-electron tomography and subtomographic average of isolated *Chlamydomonas* SNAP-DRC4 axonemes labeled with streptavidin-nanogold. Electron Microscopy Data Bank. https://www.ebi.ac.uk/pdbe/entry/emdb/EMD-20341. Deposited 25 June 2019.
53. L. Gui *et al*., The nexin-dynein regulatory complex (N-DRC) from the cryo-electron tomography and subtomographic average of isolated *Chlamydomonas* DRC5-SNAP axonemes labeled with streptavidin-nanogold. Electron Microscopy Data Bank. https://www.ebi.ac.uk/pdbe/entry/emdb/EMD-20821. Deposited 13 October 2019.